CHEMISTRY

A high-spin ground-state donor-acceptor conjugated polymer

A. E. London[1], H. Chen[2]*, M. A. Sabuj[3], J. Tropp[1], M. Saghayezhian[4], N. Eedugurala[1], B. A. Zhang[1], Y. Liu[5], X. Gu[1], B. M. Wong[6], N. Rai[3], M. K. Bowman[2], J. D. Azoulay[1]†

Interest in high-spin organic materials is driven by opportunities to enable far-reaching fundamental science and develop technologies that integrate light element spin, magnetic, and quantum functionalities. Although extensively studied, the intrinsic instability of these materials complicates synthesis and precludes an understanding of how fundamental properties associated with the nature of the chemical bond and electron pairing in organic materials systems manifest in practical applications. Here, we demonstrate a conjugated polymer semiconductor, based on alternating cyclopentadithiophene and thiadiazoloquinoxaline units, that is a ground-state triplet in its neutral form. Electron paramagnetic resonance and magnetic susceptibility measurements are consistent with a high-to-low spin energy gap of 9.30×10^{-3} kcal mol^{-1}. The strongly correlated electronic structure, very narrow bandgap, intramolecular ferromagnetic coupling, high electrical conductivity, solution processability, and robust stability open access to a broad variety of technologically relevant applications once thought of as beyond the current scope of organic semiconductors.

INTRODUCTION

Organic semiconductors (OSCs) with open-shell diradical character have degenerate or near-degenerate frontier molecular orbitals (MOs), weakly interacting unpaired electrons, efficient spin delocalization throughout the conjugated structure and show considerable narrowing of the energy gap (ΔE) between spin states (*1*, *2*). The unique electronic structures and spin-correlated phenomena, arising from unpaired electron densities and the presence of magnetic moments coupled to light elements, offer richer categories of behavior than in closed-shell OSCs. For example, these materials exhibit distinct optical, electronic, spin, and excited-state properties whose structure and dynamics can be optimized for applications in organic electronics, spintronics, nonlinear optics, and energy conversion and storage (*2*–*6*). High-spin ground states offer new notions of spin manipulation, organic magnetism, quantum functionalities, and interrelated (opto)electronic properties at the forefront of research efforts in diverse fields such as chemistry, materials science, and condensed matter physics. In contrast to inorganic materials, OSCs offer the possibility to tailor molecular and electronic structure, spin-spin interactions, and magnetic properties through chemical synthesis; enable low-cost fabrication; and exhibit advantageous phenomena such as weaker spin-orbit coupling (*7*–*9*). There are, however, only a few reports of high-spin molecules with isolable stability (*9*, *10*), and their implementation into emerging technologies is predicated on design principles that overcome their intrinsic chemical reactivity, enables straightforward synthetic manipulation, and combines the rich electronic and optical properties found in OSCs.

Prototypical classes of open-shell OSCs include polycyclic aromatic hydrocarbons and related structures, quinoidal oligothiophenes, conjugated polymers (CPs), and polyradicals such as nanographenes and zigzag edge graphene nanoribbons (ZGNRs) (*1*–*3*, *11*–*18*). These materials contrast with those that incorporate widely used spin-carrying units, which are molecular in nature and localized (*1*, *2*). In nearly all cases, the interacting electrons are in a spin-paired singlet state (spin quantum number, $S = 0$) owing to dynamic spin polarization (*16*, *19*). Intramolecular ferromagnetic (FM) coupling and inversion of the energy of spin pairing are achieved when MOs are spatially coincident, so that a parallel spin alignment reduces Coulomb repulsion, a manifestation of the Pauli exclusion principle. High-spin organics ($S \geq 1$) are generally synthesized through photochemical or redox reactions on topologically prearranged precursors, resulting in materials with half-filled degenerate MOs exhibiting strong exchange coupling mediated through bonds in close proximity (*8*, *20*). Synthetic efforts over much of the 20th century have resulted in the elucidation of molecular and topological features affecting exchange interactions, the synthesis of high-spin multiplicity organic materials, long-range magnetic ordering demonstrated in a polyarylmethyl scaffold (*21*), and the development of stable triplet diradicals that are thermally robust and amenable to sublimation (*9*, *10*). Despite these achievements, nearly all high-spin organic molecules are unstable, highly localized, and offer limited flexibility in molecular design (*8*, *9*, *22*).

Consequently, there remains a need for bottom-up chemical approaches that combine electron delocalization, electronic structure control, and intramolecular FM exchange coupling in organic materials systems. A requisite for open-shell character is the presence of unpaired spins, and intramolecular high-spin states are hypothesized to be stabilized in diradicals with extended π systems and narrow bandgaps (*20*, *23*). Kekulé-type delocalized diradicals offer promising synthetic handles by which to achieve electronically correlated midscale molecular systems. General design guidelines involve embedding nonaromatic quinoidal core structures into a π framework, which upon aromatization (at the expense of diminishing the covalency of a π bond) results in resonance stabilization of the diradical form and a degenerate partially occupied orbital manifold (*16*, *20*). The diradical character can also be controlled by the amount of resonance energy

[1]Center for Optoelectronic Materials and Devices, School of Polymer Science and Engineering, The University of Southern Mississippi, Hattiesburg, MS 39406, USA. [2]Department of Chemistry & Biochemistry, The University of Alabama, Tuscaloosa, AL 35487-0336, USA. [3]Dave C. Swalm School of Chemical Engineering and Center for Advanced Vehicular Systems, Mississippi State University, Mississippi State, MS 39762, USA. [4]Department of Physics and Astronomy, Louisiana State University, Baton Rouge, LA 70803, USA. [5]Molecular Foundry, Lawrence Berkeley National Laboratory, One Cyclotron Road, Berkeley, CA 94720, USA. [6]Department of Chemical and Environmental Engineering and Materials Science and Engineering Program, University of California, Riverside, Riverside, CA 92521, USA.
*Present address: Analytical & Testing Center, Sichuan University, Chengdu 610064, China.
†Corresponding author. Email: jason.azoulay@usm.edu

gained, substituent and structural effects, spatial distribution of the frontier MOs and generally increases as the bandgap is reduced as a result of increased configuration mixing (*11*). Design strategies aimed at the protection of spin centers with steric hindrance and delocalization of the unpaired electrons have resulted in air- and temperature-stable diradicals (*6*). Achieving narrow bandgap open-shell organic molecules generally requires large π systems, which are difficult to synthesize, isolate, and whose properties are difficult to control. This is exemplified through persistent difficulties in the solution-based synthesis of highly conjugated open-shell materials such as nanographenes, ZGNRs, and polyrylenes. These suffer from complex and protracted multistep synthetic approaches, poor solubility, and high reactivity of the open-shell intermediates. This necessitates the use of surface-mediated synthesis under ultrahigh vacuum conditions to generate large (polymeric) structures, precluding measurements of intrinsic molecular properties and practical implementation into thin-film, nanostructured, and solution-processed technologies (*12*, *13*, *15*, *17*, *24*). Furthermore, the topological modulation of exchange coupling (*J*) requires design paradigms that also consider the magnetic interaction mechanism, transmission along the π system, the Coulomb and Pauli repulsion, electrostatics, nuclear attraction, and that take higher-order electronic and quantum mechanical correlations into account (*25*). These interrelated factors in extended π systems often times negate the application of qualitative rules of orbital occupation and spin alignment conventionally applied to smaller molecular systems with well-defined topologies. As such, a neutral high-spin OSC accessed using conventional synthetic approaches has yet to be demonstrated by experiment.

OSCs with embedded quinoidal subunits, extensive delocalization, and very narrow bandgaps have demonstrated open-shell electronic configurations in their neutral form, a property which has also recently been demonstrated in narrow bandgap donor-acceptor (DA) molecules and copolymers (*14*, *18*, *26*). DA CPs composed of alternating in chain strong-donor and strong-acceptor interactions have demonstrated utility as active components in (opto)electronic technologies since they interact with light, transport charges, offer high chemical stability, and can be readily tuned through chemical modification. The chemical, electronic, and structural heterogeneities that affect the degree of correlation and conformational disorder in these materials complicate bandgap control at low energies, the development of design rules that favor open-shell ground states, and the application of quantum chemical approaches. These complexities motivated our investigation of design strategies, which may favor and better stabilize high-spin ground states in π-extended systems.

RESULTS

Synthesis of a high-spin DA CP

Here, we address a core challenge in the development of high-spin OSCs with long-range π-electron correlations, interrelated (opto)electronic functionalities, and robust stability. We synthesized poly(4-(4-(3,5-didodecylbenzylidene)-4*H*-cyclopenta[2,1-*b*:3,4-*b*′]dithiophen-2-yl)-6,7-dimethyl-[1,2,5]-thiadiazolo[3,4-*g*]quinoxaline), a DA CP that overcomes conjugation saturation behavior, exhibits a very narrow bandgap (E_g < 0.6 eV), and is a ground-state triplet (Fig. 1). A salient design feature is the cross-conjugated donor, which allows intricate control of structure-property relationships, raises the highest occupied MO (HOMO), affords adjustments to molecular indices such as bond length alternation (BLA), and promotes a highly planar conjugated backbone (see the Supplementary Materials) (*27*, *28*). The strong, proquinoidal thiadiazoloquinoxaline (TQ) acceptor is key for lowering the lowest unoccupied MO (LUMO) and promoting strong electron correlations to form and stabilize unpaired spins in the long-chain limit. We synthesized the polymer using a microwave-assisted Stille cross-coupling copolymerization between (4-(3,5-didodecylbenzylidene)-4*H*-cyclopenta[2,1-*b*:3,4-*b*′]dithiophene-2,6-diyl)bis-(trimethylstannane) (**M1**) and 4,9-dibromo-6,7-dimethyl[1,2,5]thiadiazolo[3,4-*g*]quinoxaline (**M2**) (Fig. 1) (*29*). Using $Pd(PPh_3)_4$ as the catalyst and a reaction time of 40 min afforded the polymer in 68% yield following purification using Soxhlet extraction. The preparation of **M1** was adapted from literature procedures with modifications outlined in Materials and Methods (figs. S1 to S4). The planar sp^2-hybridized aryl-olefin functionality allows strategic placement of $-C_{12}H_{25}$ substituents that promote solubility, afford direct coupling of the donor and acceptor components, and participate in the overall stability of the structure through kinetically blocking reactive sites. Gel permeation chromatography (GPC) at 160°C in 1,2,4-trichlorobenzene showed a number average molecular weight (M_n) of 15 kg mol^{-1} and dispersity ($Đ$) of 1.50 under these conditions.

Solid-state properties of polymer thin films

The high solubility in common organic solvents enables solution processing, and we prepared thin films by spin-coating a chlorobenzene solution (10 mg ml^{-1}) of the polymer onto NaCl substrates. The polymer demonstrates a broad absorption profile with an absorption maximum (λ_{max}) of 1.30 μm and measureable absorbance extending past 7 μm in the solid state (Fig. 2A). The optical bandgap (E_g^{opt}) is less than 0.30 eV, as estimated from the absorption onset of the thin film. An exact determination is difficult as a result of vibrational features superimposed on the electronic absorption tail, particularly at 0.1 to 0.2 eV

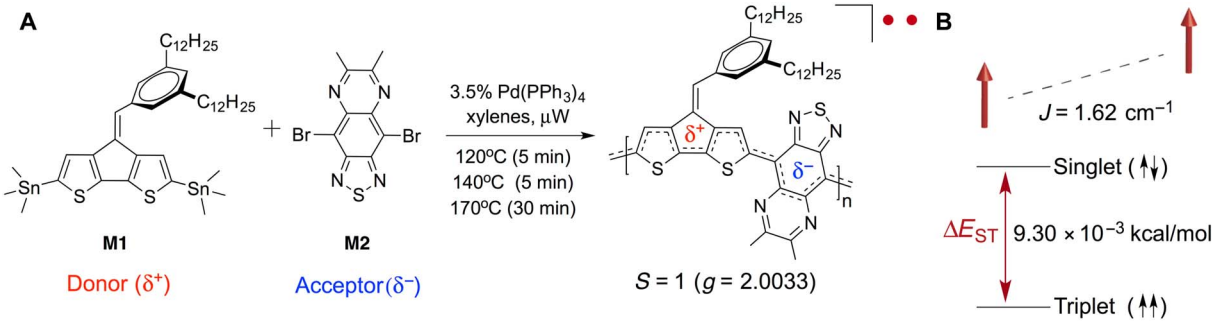

Fig. 1. Synthesis of high-spin DA CP using a Stille cross-coupling copolymerization reaction. (**A**) The molecular building blocks and rapid polymerization approach used to synthesize the polymer. (**B**) Measured magnetic properties exhibiting intramolecular FM exchange coupling and a high-to-low spin energy gap of 9.30 × 10^{-3} kcal mol^{-1}.

(~800 to 1600 cm^{-1}). Cyclic voltammetry (CV) shows that the HOMO is located at −4.79 eV and that the LUMO is at −4.23 eV, which gives an electrochemical bandgap (E_g^{elec}) of 0.56 eV (Fig. 2C). These data demonstrate that this particular DA combination yields a dramatic reduction in the bandgap when compared to other closely related substitution patterns. For example, poly(4-(4,4-dihexadecyl-4*H*-cyclopenta[2,1-*b*:3,4-*b*′]dithiophen-2-yl)-6,7-dimethyl[1,2,5]thiadiazolo[3,4-*g*]quinoxaline), which differs only in the donor bridgehead substitution pattern and solubilizing alkyl chains, exhibits E_g^{opt} = 0.57 eV and E_g^{elec} = 1.03 eV (*30*). The extensive π conjugation is evident from a bandgap that is among the lowest obtained for solution-processable conjugated materials and comparable to the longest oligorylene (E_g^{opt} = 0.47 eV) and porphyrin arrays (E_g^{opt} = 0.18 eV), which overcome conjugation saturation behavior through covalent fusion of the backbone (*24*, *31*).

Grazing-incidence wide-angle x-ray scattering (GIWAXS) indicates a largely disordered morphology as evidenced by the absence of higher-order diffraction peaks from alkyl chains (Fig. 2B). The weakly crystalline domain adopts a face-on orientation as indicated from the (010) scattering peak. A broad peak at a scattering vector (q) value of ~1.79 $Å^{-1}$ corresponds to an intermolecular ordering (π-π stacking) distance of ~3.51 Å between polymer chains. A low q peak (0.246 $Å^{-1}$) with no higher-order Bragg reflections exists corresponding to a d-spacing of ~25.5 Å, indicative of weakly ordered lamellar packing of the polymer side chains. Charge transport measurements show linear current-voltage (*I*-*V*) characteristics consistent with an intrinsic electrical conductivity (σ) of ~10^{-2} S cm^{-1} in the absence of dopants (Fig. 2D). This exceeds some of the best values reported for very narrow bandgap charge-neutral molecular systems and self-doped DA CPs (*30*, *32*, *33*). Repeated measurements of the *I*-*V* characteristics and electrochemical sweeps demonstrate the chemical robustness of this material (fig. S5). Thermogravimetric analysis (TGA) suggests that thermal decomposition begins at ~375°C (fig. S6).

Electron paramagnetic resonance and magnetic susceptibility measurements

We studied the magnetic properties by electron paramagnetic resonance (EPR) spectroscopy (in frozen xylenes) and superconducting quantum interference device (SQUID) magnetometry of a solid sample. The EPR measurement displayed a broad single line (5 to 10 gauss wide) at a g factor (g) of 2.0033, whose intensity increased with cooling, indicating a paramagnetic ground state (Fig. 3A). The data were fit to the Bleaney-Bowers equation in the range of 4 to 25 K with a singlet-triplet energy gap (ΔE_{ST}) of 9.30×10^{-3} kcal mol^{-1} (J = 1.62 cm^{-1}) consistent with weak FM coupling ($J > 0$) between spins (Fig. 3B) (*34*). Variable temperature (3 to 225 K) magnetic susceptibility measurements via SQUID revealed that the magnetic susceptibility (χ) decreased as temperature increased (Fig. 3C), consistent with EPR. A Curie-Weiss analysis on the χ versus T data gave a mean-field parameter (θ) of 0.93 K, which demonstrates that the ground state is independent of spin concentration and indicates weak intermolecular FM interactions. The magnetization (M) versus magnetic field (H) plots at 2, 3, and 5 K were

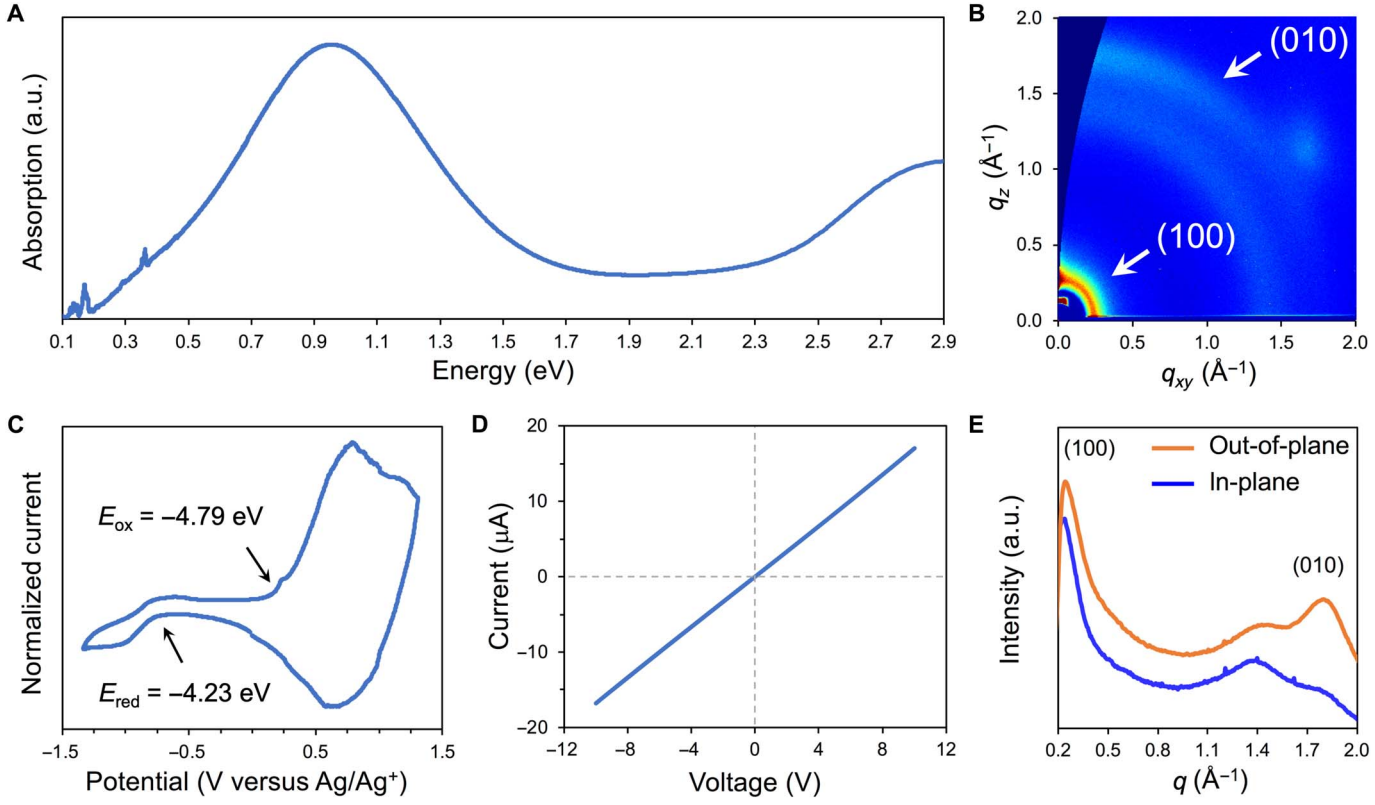

Fig. 2. Solid-state properties of polymer thin films. (**A**) Absorption spectra of thin film cast from chlorobenzene onto a NaCl substrate and (**B**) two-dimensional GIWAXS profile obtained using the same processing conditions and a silicon substrate. (**C**) CV indicates a HOMO-LUMO energy gap of 0.56 eV. (**D**) Current-voltage characteristics in a 30-μm channel with σ of ~10^{-2} S cm^{-1}. (**E**) One-dimensional line cuts of the integrated in-plane and out-of-plane two-dimensional GIWAXS profile mainly showing a peak at q ~1.79 $Å^{-1}$ that is related to interchain spacing of 3.51 Å. a.u., arbitrary units.

fit to a modified Brillouin function, resulting in $S = 0.94$, which is very close to $S = 1$ and consistent with a triplet ground state (Fig. 3D). The χT versus T plot (Fig. 3C, inset) is flat across a wide temperature range of up to 225 K, consistent with Curie paramagnetism and previous reports of high-spin organic systems (*8*, *35*).

The small singlet-triplet gap provides an efficient pathway for electron spin-lattice relaxation through the Orbach-Aminov relaxation mechanism in which a lattice vibration or phonon thermally excites the triplet state into the singlet, followed by decay back to the triplet (*36*). The phonon energy must be resonant with the singlet-triplet gap and the number of such phonons is governed by the Boltzmann distribution, so that the temperature dependence of electron spin-lattice relaxation gives an independent measure of ΔE_{ST}. Spin-lattice relaxation was directly measured by pulsed EPR between 10 and 80 K at X band using a saturation recovery method with a broadband (>120 MHz) picket fence (Fig. 3E) (*37*). The recovery of the pulsed EPR signal from 10^{-7} to 10^{-2} s after saturation was measured from the two-pulse spin echo. The recoveries showed a minor, slowly relaxing component that we attribute to free radical impurities or frustrated states in the polymer. Fits of Eq. 1 to the recovery of the major signal were excellent with residuals less than 0.3% (Fig. 3E).

$$M_Z(t) - M_{Z,eq} = (M_Z(0) - M_{Z,eq})e^{-bt} \quad (1)$$

The b parameter in Eq. 1 is the electron spin-lattice relaxation rate ($1/T_{1e}$) of the triplet state. The temperature dependence of $1/T_{1e}$ is described well by the Orbach-Aminov relaxation process with $\Delta E_{ST} = 9.30 \times 10^{-3}$ kcal mol^{-1} ($2J/k_B = 4.67$ K, where k_B is the Boltzmann constant) confirming the spin susceptibility measurements.

The two-pulse spin echo measurements of instantaneous diffusion in which the decay rate changes with microwave power are consistent with weakly coupled spins (*38*). The ratio of the spin echo decays at the two-pulse powers differing by 12 dB was fit with Eq. 2 (Fig. 3F).

$$\ln(V_1(\tau)/V_2(\tau)) = a_0 - k\tau^{(d/3)} \quad (2)$$

The coefficient d is the fractal dimensionality of the spatial distribution of electron spins. The d values at different temperatures are all close to 1, which indicates that the nearest electron spins are approximately distributed in one dimension, as if randomly placed on a linear polymer chain. For electron spins that can distribute in three dimensions ($d = 3$), such a plot produces a straight line, rather than the distinct curve seen here (Fig. 3F). Therefore, the magnetic measurements all indicate that the polymer is a ground-state triplet. EPR measurements of a solid sample stored at room temperature under a nitrogen atmosphere showed no discernable changes over a period of 30 days (fig. S6).

Quantum chemical calculations

Density functional theory (DFT) calculations at the unrestricted (U)B3LYP/6-31G** level of theory on model oligomer systems were used to understand the evolution of the electronic structure as calculations

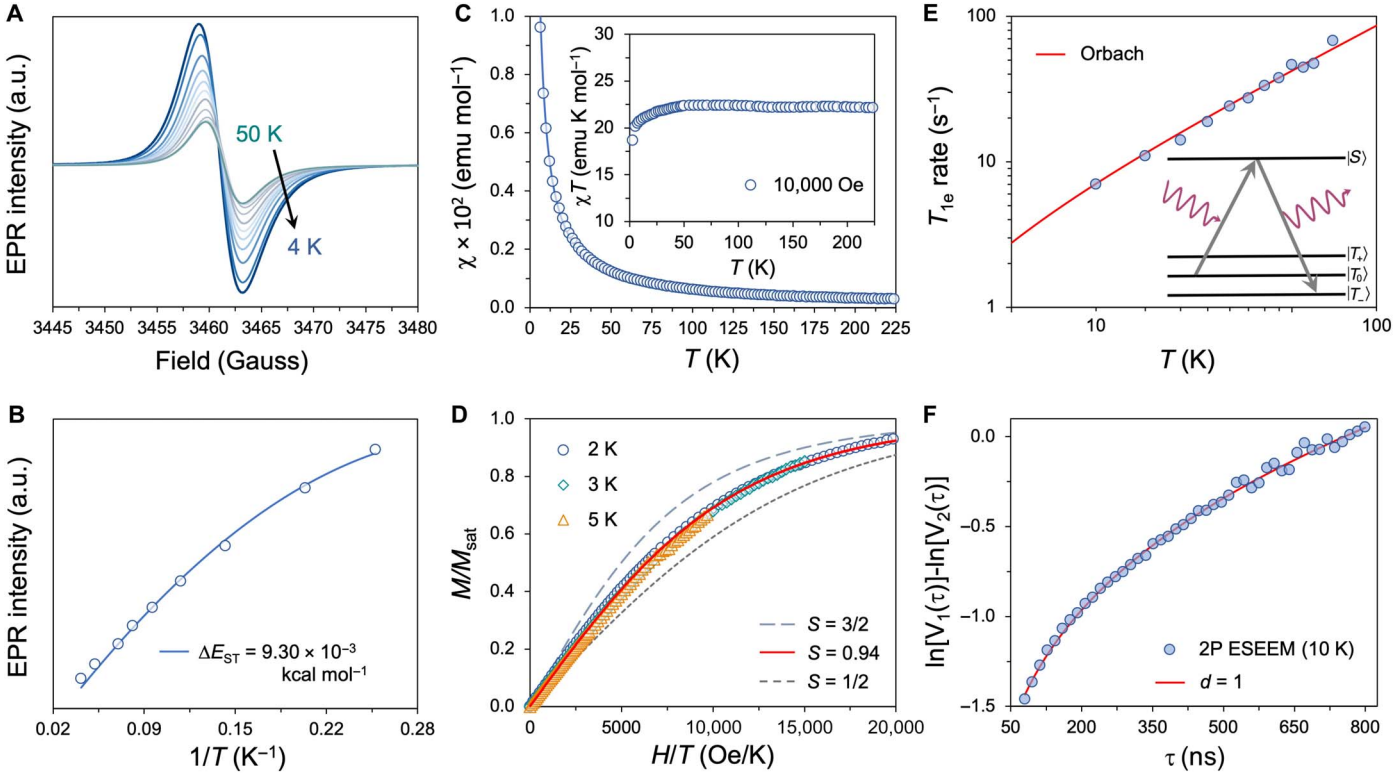

Fig. 3. Magnetic properties of the polymer. (**A**) EPR (X band) spectra from 4 to 50 K and (**B**) temperature-dependent fit to the Bleaney-Bowers equation with ΔE_{ST} of 9.30×10^{-3} kcal mol^{-1}. (**C**) SQUID magnetometry of solid sample. Main plot: Magnetic susceptibility, χ versus T, from 3 to 225 K fit to the Curie-Weiss law (blue line). Inset: Observed χT versus T dependence. (**D**) Magnetic field (H) dependence of the magnetization (M) at 2, 3 and 5 K, plotted as M/M_{sat} versus H, with Brillouin functions for $S = 1/2$, 0.94, and 3/2. (**E**) Log-log plot of the X band $1/T_{1e}$ recovery rates versus temperature fit by the temperature dependence of the Orbach-Aminov process with an energy gap of 4.67 K. (**F**) Two-pulse electron spin echo instantaneous diffusion data at 10 K indicate a one-dimensional spin distribution ($d = 1$) along a linear chain. ESEEM, electron spin echo envelope modulation.

on oligomers larger than eight repeat units (n) proved intractable. The dimer (n = 2) exhibits a closed-shell ground state and mixed aromatic-quinoidal bonding pattern as a result of the strong TQ acceptor (fig. S11 and table S5). For the trimer (n = 3), the open-shell (unrestricted) solution becomes lower in energy than the closed-shell, indicating that the diradical form contributes to the ground state. BLA analysis and nucleus-independent chemical shift (NICS) calculations show molecular features associated with the evolution of open-shell character as a function of conjugation length (figs. S7 to S15 and tables S2 to S9). These include an increase in the quinoidal character of the oligomer core, enhanced delocalization into ancillary TQ pyrazine rings, and a concomitant lengthening of long acceptor bonds in the conjugated backbone (*16*). The contribution of the open-shell resonance form to the ground-state structure is described by the diradical character index ($0 < y < 1$), which increases rapidly with oligomer length (y = 0.13 → 0.91 from n = 3 → 8), and implies formation of a pure diradical (y = 1) at longer chain lengths (table S2) (*24*, *39*). This trend is accompanied by a progressive localization of the α and β singly occupied MOs (SOMOs) of the singlet to opposite sides of the oligomer as the chain length is increased. As a result, the two electrons with antiparallel spins are permitted to correlate in separate spaces (Fig. 4A), which further diminishes the covalency of the singlet, increases y, and progressively mitigates electron repulsion. The sites of highest spin density shown for the singlet octamer (Fig. 4B) indicate separation of spins from a quinoidal interior to the oligomer periphery, consistent with a delocalized singlet diradical. This phenomenon draws analogy to other π-extended open-shell systems such as quinoidal polythiophenes, p-quinodimethanes, and rylene ribbons but has not been reported in a DA CP (*24*, *40*, *41*). Additional calculations on model oligomer systems with various substitution patterns demonstrate that y, ΔE_{ST}, and interactions between correlated electrons of these open-shell DA diradicals can be achieved (fig. S16).

A small HOMO-LUMO gap inherent to the polymer allows admixing of the HOMO and LUMO in the ground state. The extent of the electron exchange interaction is evident as ΔE_{ST} rapidly decreases (ΔE_{ST} = −0.18 → −0.02 eV from n = 3 → 8; table S2). Experimental values for the bandgap (E_g^{DFT} = 0.77 eV; table S2) and ΔE_{ST} lower than those calculated demonstrate that these calculations do not offer a comprehensive assessment of the polymeric system. However, a linear extrapolation of E_g^{DFT} versus $1/n$ to the polymer limit ($n \to \infty$) is consistent with experimental results (fig. S7A). The question is then whether the exchange coupling favoring the triplet is sufficient to overcome the "covalent" character of the singlet. The rapid increase in y and the almost saturated ($y \to 1$) value at n = 8 indicate that the spins are less electronically coupled. Extrapolation of these data (fig. S7B) indicates that an inflection point is achieved at n = ~13, corresponding to an M_n of ~11 kg mol^{-1}, lower than the value obtained by GPC. As the conjugation length increases, so does the spacing between the unpaired electrons in the triplet (Fig. 4C), leading to reduced Coulomb repulsion. The spin density distribution (n = 8) in the singlet indicates extensive spin polarization and delocalization over the whole π system (Fig. 4B), while the triplet (Fig. 4C) becomes progressively more localized. Thus Coulomb repulsion in the singlet (where the unpaired electrons are permitted to delocalize over the same region of space) remains higher at longer chain lengths, likely stabilizing the triplet as the ground state in the long-chain limit (*42*).

DISCUSSION

Bottom-up approaches to access and tune the properties of large open-shell π systems with correlated ground states are critically important in

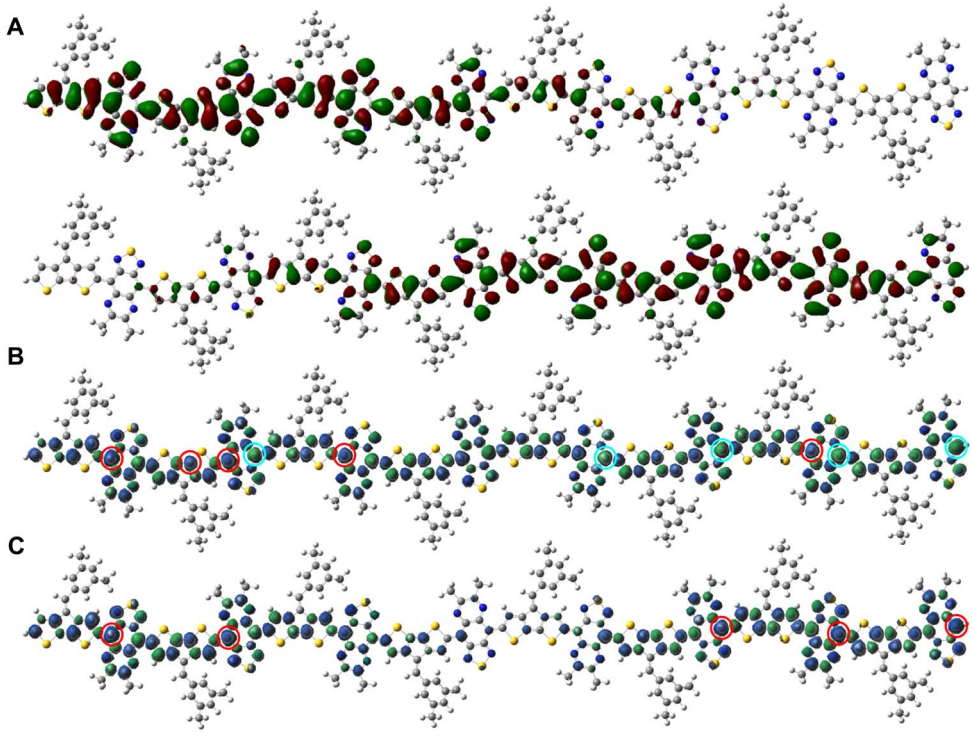

Fig. 4. Electronic structure of the oligomer (n = 8) at the UB3LYP/6-31G level of theory.** (**A**) Calculated α-SOMO (top) and β-SOMO (bottom) profiles of the open-shell singlet. (**B**) Spin density distribution of the singlet and (**C**) triplet states with most probable locations for the unpaired electrons highlighted with open circles (red, up spin; blue, down spin).

advancing the understanding of the relationship between molecular structure, electronic topology, and the achievable collective properties of complex material systems. These materials are generally unstable owing to their electron-rich nature and highly localized radical sites. In our polymer, there is a significant internal charge transfer character between electron-rich and electron-deficient components throughout the π framework. Furthermore, both the singlet and triplet states are essentially degenerate and indicate extensive delocalization of the spin density, a requisite for thermodynamic stabilization. This picture differs from electron-rich nanographenes or ZGNRs, which localize unpaired electrons at the zigzag edges (*12*, *13*, *15*). Furthermore, the spin-spin interactions and alignment (exchange) in these midscale molecular systems can be controlled through diverse synthetic handles, which are less energetically costly as *n* increases. Collectively, these results demonstrate that DA CPs provide a unique pathway to strong electron correlations, control of the bandgap at very low energies, and approaches to forming electronic states that span the entire range from closed-shell singlets to biradicaloids ($0 < y < 1$) with varying amounts of open-shell character and to biradicals ($y = 1$) in both singlet ($S = 0$) and triplet ($S = 1$) spin states. We anticipate that the combination of straightforward synthesis and modularity will enable the practical development of materials with complex and tunable electronic structures, varying magnitudes of intramolecular electron-electron pairing, cooperative electronic properties based on π electrons, and controlled spin alignments—design paradigms that underlie the development of next-generation (opto)electronic technologies. The robust stability, solution processability, and interrelated properties also afford a platform for implementation of high-spin organic materials into a diversity of new devices. This will allow us and others to elucidate complex physical mechanisms that underlie emergent phenomena such as those associated with spin-based magnetic properties and quantum electronic devices.

MATERIALS AND METHODS

General remarks

Manipulations of air- and moisture-sensitive compounds were carried out under an inert atmosphere in a nitrogen-filled glovebox or using standard Schlenk techniques. Reagents, unless otherwise specified, were purchased from Fisher Scientific and used without additional purification. Xylenes, chlorobenzene, 1,2-dichlorobenzene, and acetonitrile were degassed and dried over 4-Å molecular sieves before use. Chloroform-*d* ($CDCl_3$) and 1,1,2,2-tetrachloroethane-d_2 ($C_2D_2Cl_4$) were purchased from Cambridge Isotope Laboratories and used as received. Tetrakis(triphenylphosphine)palladium(0) was purchased from Strem Chemicals and used without further purification. 2,6-Dibromo-4*H*-cyclopenta[2,1-*b*:3,4-*b*′]dithiophen-4-one and **M2** were prepared according to previously reported procedures (*27*, *29*). **M1** was prepared using an optimized multigram scale synthetic procedure (fig. S1). ^{1}H and ^{13}C nuclear magnetic reasonance (NMR) spectra were collected on a Bruker Avance III 600 MHz spectrometer, and chemical shifts, δ [in parts per million (ppm)], were referenced to the residual solvent impurity peaks (figs. S2 to S4). Data are reported as s (singlet), d (doublet), t (triplet), m (multiplet), and br (broad), and coupling constants (*J*) are reported in hertz. Flash chromatography was carried out on a Teledyne ISCO CombiFlash Purification System using RediSep Rf prepacked columns. Microwave-assisted polymerization reactions were performed using a CEM Discover microwave reactor. The number average molecular weight (M_n) and dispersity (*Đ*) of the polymer were determined by GPC relative to polystyrene standards at 160°C in 1,2,4-trichlorobenzene (stabilized with 125 ppm of butylated hydroxytoluene) in an Agilent PL-GPC 220 high-temperature GPC system with four PLgel 10-μm MIXED-B columns. Polymer samples were prepared at a concentration of 1 to 2 mg ml^{-1} in 1,2,4-trichlorobenzene at 160°C.

Monomer synthesis

(3,5-Didodecylphenyl)methanol (1)

3,5-Didodecylbenzaldehyde (11.21 g, 25.3 mmol) was dissolved in a mixture of methylene chloride (60 ml) and ethanol (60 ml) under nitrogen. Sodium borohydride (3.83 g, 101 mmol) was added in five portions (5 × 20.2 mmol) at room temperature over the course of 20 min. After stirring for 16 hours at room temperature, the reaction was quenched with 1 M HCl (120 ml) and the mixture was poured into a separatory funnel. The aqueous layer was removed, and the organic phase was washed with $NaHCO_3$ (1 × 100 ml) and water (2 × 100 ml). The organic layer was then washed with brine (1 × 100 ml), dried over anhydrous $MgSO_4$, and filtered through a pad of celite. Volatiles were removed in vacuo, and purification was accomplished by flash chromatography using a hexanes:ethyl acetate gradient, affording 10.25 g of a white solid (23.1 mmol, 91%). Data are as follows: ^{1}H NMR (600 MHz, chloroform-*d*): δ 7.01 (2H, s), 6.95 (1H, s), 4.64 (2H, d, J = 5.1 Hz), 2.60 (4H, t, J = 7.9 Hz), 1.79 (1H, t, J = 5.6 Hz), 1.63 (4H, m), 1.25 to 1.40 (36H, m), 0.91 (6H, t, J = 6.7 Hz); ^{13}C NMR (151 MHz, chloroform-*d*): δ 143.37, 140.89, 128.09, 124.53, 65.70, 36.09, 32.09, 31.70, 29.84, 29.78, 29.69, 29.60, 29.52, 22.85, 14.25. Mass spectrometry (MS) [electrospray ionization (ESI)] exact mass calculated for $C_{31}H_{56}O$ is as follows: *m/z* 445.4409 ($[M^+] + [H^+]$) and 445.4195 (found).

1-(Bromomethyl)-3,5-didodecylbenzene (2)

(3,5-Didodecylphenyl)methanol (**1**) (8.51 g, 19.1 mmol) was dissolved in anhydrous methylene chloride (100 ml) under nitrogen and cooled in an ice bath. PBr_3 (2.80 ml, 29.5 mmol) was added dropwise using an addition funnel. The reaction mixture was allowed to slowly warm to room temperature and stirred for 16 hours. The reaction mixture was subsequently cooled in an ice bath and carefully quenched with deionized (DI) water. The mixture was transferred to a separatory funnel and extracted with 50 ml of methylene chloride. The organic layer was washed with saturated $NaHCO_3$ (1 × 100 ml), water (2 × 100 ml), brine (1 × 100 ml) and dried over anhydrous $MgSO_4$. Solvents were removed in vacuo, and purification by flash chromatography using hexanes as the eluent gave 7.77 g of colorless oil, which solidified upon standing (15.3 mmol, 80%). Data are as follows: ^{1}H NMR (600 MHz, chloroform-*d*): δ 7.05 (2H, s), 6.96 (1H, s), 4.48 (2H, s), 2.60 (4H, t, J = 7.9 Hz), 1.64 (4H, m), 1.25 to 1.40 (36H, m), 0.93 (6H, t, J = 6.7 Hz); ^{13}C NMR (151 MHz, chloroform-*d*): δ 143.57, 137.61, 128.94, 126.54, 35.96, 34.16, 32.11, 31.55, 29.86, 29.84, 29.83, 29.77, 29.67, 29.55, 29.54, 22.86, 14.27. MS (ESI) exact mass calculated for $C_{31}H_{55}Br$ is as follows: *m/z* 507.3565 ($[M^+ + H^+]$) and 507.3728 (found).

2,6-Dibromo-4-(3,5-didodecylbenzylidene)-4H-cyclopenta[2,1-b:3,4-b′]dithiophene (3)

1-(Bromomethyl)-3,5-didodecylbenzene (**2**) (5.60 g, 11.0 mmol) and triphenylphosphine (3.04 g, 11.6 mmol) were added to an oven-dried flask equipped with a stir bar. The flask was purged with nitrogen and then sealed. Toluene (50 ml) was added, and the mixture was heated to reflux for 12 hours. After cooling, the solvent was removed in vacuo, leaving a waxy white solid. The flask was brought inside the glovebox, and 2,6-dibromo-4*H*-cyclopenta[2,1-*b*:3,4-*b*′]dithiophen-4-one (3.67 g, 10.5 mmol), 35 ml of anhydrous ethanol, and 50 ml of chloroform were added. The reaction mixture was heated to 60°C

and stirred for 30 min to fully dissolve the contents. A 60°C solution (1.1 M) of sodium ethoxide (1.13 g, 16.5 mmol) in 15 ml of anhydrous ethanol was added, resulting in a deep red solution. The reaction mixture was stirred for 16 hours at 60°C and then cooled to room temperature, quenched with 100 ml of DI water, and extracted with 100 ml of methylene chloride. The organic layer was washed with water (2 × 100 ml) brine (1 × 100 ml), and then dried over anhydrous $MgSO_4$. Solvents were removed in vacuo, and purification by flash chromatography using pentane as the eluent afforded 5.37 g of a red oil that solidified upon standing (7.06 mmol, 71%). Characterization was consistent with what was previously reported (*27*).

Polymer synthesis

A microwave tube was loaded with **M1** (150 mg, 0.162 mmol) and **M2** (57.8 mg, 0.155 mmol). The tube was brought inside the glovebox, and 750 µl of a $Pd(PPh_3)_4$/xylenes stock solution (3.5 mol%) was added. The tube was sealed and subjected to the following reaction conditions in a microwave reactor with stirring: 120°C for 5 min, 140°C for 5 min, and 170°C for 30 min. After this time, the reaction was allowed to cool, leaving a solid gelled material. The mixture was precipitated into methanol and collected via filtration. The residual solid was loaded into an extraction thimble and washed successively (under a N_2 atmosphere and in the absence of light) with methanol (2 hours), acetone (2 hours), hexanes (2 hours), a 1:1 mixture of hexanes and tetrahydrofuran (12 hours), and then acetone (2 hours). The polymer was dried in vacuo to give 85 mg (68%) of a black solid. Data are as follows: M_n = 15.0 kg mol^{-1} and $Đ$ = 1.50; ^{1}H NMR (600 MHz, 1,1,2,2-tetrachloroethane-d_2, 398 K): δ 8.00 to 6.50 (6H, br m), 3.60 to 2.50 (4H, br m), 2.30 to 1.15 (40H, br m), 1.10 to 0.80 (6H, br m), 0.72 (6H, s); absorption: λ_{max} (solution, 1,2-dichlorobenzene, 25°C) = 1.25 µm, λ_{max} (thin film) = 1.30 µm, and ε = 16,057 liters mol^{-1} cm^{-1}.

Inductively coupled plasma optical emission spectroscopy

Elemental concentrations of tin, iron, and palladium were measured in two separately prepared polymer samples. Sample (10 mg) was calcined overnight at 500°C and subsequently digested in aqua regia for 12 hours. Analysis was performed in a PerkinElmer Optima 2100 DV inductively coupled plasma optical emission spectrometer.

UV-Vis-NIR and FTIR spectroscopy

Ultraviolet-visible (UV-Vis) and Fourier transform infrared (FTIR) spectra were recorded from 0.375 to 3.30 µm and from 3.30 to 12.40 µm using a PerkinElmer LAMBDA 950 UV-Vis spectrometer and a Bruker VERTEX 80 FTIR spectrometer, respectively. Thin films were prepared by spin-coating a chlorobenzene solution (10 mg ml^{-1}) of the polymer onto NaCl substrates at 800 rpm for 60 s. Solution spectra were recorded from 0.375 to 2.25 µm using a Cary 5000 UV-Vis-NIR spectrophotometer in dry 1,2-dichlorobenzene at room temperature.

Electrochemistry

CV (50 mV s^{-1}) was used to determine the electrochemical characteristics of drop-cast films of the polymer at room temperature in degassed anhydrous acetonitrile with tetrabutylammonium hexafluorophosphate (0.1 M) as the supporting electrolyte. The working and counter electrodes were platinum wires, and the reference electrode was Ag/AgCl. The reference electrode was calibrated with ferrocene after each measurement, and the potential axis was corrected to the normal hydrogen electrode (NHE) using −4.75 eV for NHE (*27*, *28*). The HOMO was estimated from the onset of oxidation, and LUMO was estimated from the onset of reduction. The bandgap was calculated from the HOMO-LUMO difference.

Grazing-incidence wide-angle x-ray scattering

GIWAXS samples were prepared by spin-coating a film from chlorobenzene (as previously described) onto a Si wafer. The samples were measured at beamline 11-3 at the Stanford Synchrotron Radiation Lightsource (SSRL), in a helium-filled chamber, at an incidence angle of 0.12°, with a Rayonix Mar CCD225 detector. The sample-to-detector distance was 300 mm. An x-ray beam wavelength of 0.9758 Å and an exposure time of 400 s were used. The data were processed using the WaveMetrics Igor Pro with a Nika script and WAXStools software.

Charge transport measurements

Charge transport measurements were evaluated using two common architectures: (i) a typical bottom-gate, top-contact organic field-effect transistor (OFET) geometry and (ii) by evaporating gold electrodes onto a thin film of the polymer on a quartz substrate. The polymer was dissolved in chloroform at 58°C to make a solution (5 mg ml^{-1}) in an N_2 atmosphere. Silicon and quartz substrates were cleaned using detergent in DI water, acetone, and then isopropyl alcohol for 15 min sequentially under sonication and then dried in an oven. The substrates were treated in a UV/ozone cleaner for 30 min. The heavily n-doped silicon substrates with a 300-nm thermally grown SiO_2 dielectric were prepared as the bottom-gate electrode. The SiO_2 dielectric was passivated with octadecyltrichlorosilane [$CH_3(CH_2)_{17}SiCl_3$]. The polymer was spin-coated onto these substrates at 1000 rpm for 60 s to give a 32-nm-thick film. In the case of the quartz substrates, a polymer solution (5 mg ml^{-1}) and 1000 rpm for 60 s were found to be optimal, resulting in a 29-nm-thick film. Gold electrodes (40 nm) were thermally evaporated at 1 × 10^{-7} torr using a shadow mask on top of the polymer film. The defined channel was 30 µm in length and 1 mm in width. Devices were tested on a Signatone probe station inside a nitrogen glovebox. Data were collected using a Keithley 4200 semiconductor characterization system. The polymer did not display the ability to reach a saturated state or demonstrate any type of ON current–to–OFF current ratio in an OFET configuration, and results were nearly identical to those obtained on a quartz substrate (fig. S5).

Thermogravimetric analysis

TGA was conducted on a TA Instruments Q500 thermogravimetric analyzer by heating from room temperature to 800°C at a heating rate of 10°C min^{-1} under a nitrogen flow of 40 ml min^{-1}. The polymer displayed good thermal stability with an onset of degradation of ~375°C and decomposition temperature (T_d) of 383°C, defined by 5% weight loss.

X-ray photoelectron spectroscopy

Chemical composition was evaluated using a Thermo Scientific ESCALAB Xi$^+$ X-ray photoelectron spectrometer. An Al anode was used as an x-ray source. Survey spectra were recorded in a 1-eV step size with a pass energy of 200 eV. Detailed scans were recorded in 0.1-eV step sizes with a pass energy of 50 eV.

SQUID magnetometry

Magnetic measurements were carried out on a Quantum Design MPMS XL SQUID magnetometer. The sample was prepared by placing 72 mg of polymer in ethyl alcohol–sonicated and ultrahigh pure nitrogen–dried

polycarbonate capsule inside a Quantum Design quartz sample holder assembly. To minimize the background contribution, the capsule was filled with the polymer; hence no tissue, wool, or Kapton tape was used. Before measurement, the background of the empty capsule was recorded. Temperature-dependent data were collected from $T = 3$ to 225 K at 1 T field cooling/warming, and field-dependent data were collected from $H = 0$ to 6 T at 2, 3, and 5 K. The χT curve was corrected for the diamagnetism of the sample holder and intrinsic diamagnetism of the sample. The data were fit to the Brillouin function, where S is the spin-quantum number and M_{sat} is the magnetization saturation.

EPR spectroscopy

Variable temperature measurements were performed using Bruker E540 or E680 EPR spectrometers operating at X band. Samples were evacuated to 40 mbar for 18 hours before measurement. The solution sample was dissolved in anhydrous degassed xylenes, and the tube sealed in a nitrogen-filled glovebox. Data were collected from 4 to 50 K for the xylenes glass. The EPR signal intensity was fit to the Bleaney-Bowers equation (Eq. 3 and Fig. 3B) from 4 to 25 K to determine the singlet-triplet energy splitting (ΔE_{ST}) (*34*) using the equation

$$I_{EPR} = \frac{C}{T}\frac{3e^{-2J/k_B T}}{1 + 3e^{-2J/k_B T}} \quad (3)$$

where C is a constant, J is the intramolecular exchange coupling constant, and $2J$ is ΔE_{ST}. A dilute solution (10^{-5} M) was used to elucidate the single-chain behavior. The diradical gives a nonlinear response, consistent with $J > 0$ (FM coupling). The best fit results in $J = 1.62$ cm^{-1} ($\Delta E_{ST} = 4.67$ K).

For the solid sample, spin-lattice relaxation was measured between 10 and 80 K at X band using a Bruker E680 spectrometer by the saturation recovery method using a picket fence for broadband saturation, with 20 pulses (3 μs apart) of 12-ns duration (3π/8 turning angle). This picket fence achieves greater than 90% saturation for EPR signals within 120 MHz of resonance and eliminates artifactual signal recovery caused not by relaxation of electron spins to the lattice but by spectral diffusion of unsaturated, off-resonance signals into resonance. The EPR signal recovery was measured from the two-pulse spin echo. In the two-pulse spin echo experiment, the two-pulse Hahn echo sequence was used (π/2-τ-π-τ-echo), and the intensity of the echo was measured as a function of τ. Most of the relaxation of the spin magnetization along the applied magnetic field (M_z) is described by Eq. 1.

Careful examination of the recovery curves showed a minor component with slow relaxation. This led us to add a second slow k. The resulting fits became much better with residuals less than 0.3%. The minor component at all temperatures is <10% and represents surface states or radical impurities. The temperature dependence of the exponential b term is described well by an Orbach-Aminov relaxation process which involves an excited spin state and two phonons (*36*).

$$\frac{1}{T_{1e}} = \frac{A}{(e^{\Delta E_{ST}/k_B T} - 1)} \quad (4)$$

Good fits were obtained with ΔE_{ST} equivalent to 4.67 K, which validates the determination of ΔE_{ST} from the Bleaney-Bowers fit.

Quantum chemical calculations

Molecular geometries for the electronic ground state (S_0) and the triplet state of the model oligomers ($n = 1$ to 8) were optimized in the gas phase using DFT with Becke's three-parameter functional B3LYP (*43*) and 6-31G** basis set. Dodecyl ($-C_{12}H_{25}$) side chains were truncated with methyl ($-CH_3$) groups. Broken-symmetry (BS) singlet-state calculations were started with a restricted wave function. $NICS_{iso}(1)$ was computed by the gauge-independent atomic orbital method on the BS-optimized geometry by a single-point energy calculation at the UB3LYP/6-31G** level of theory by placing a ghost atom at 1 Å perpendicularly above the ring plane to account for only the π-electron contribution. At this distance, the contribution of the π electrons was maximized (*44*). The diradical index y was calculated at UB3LYP/6-31G** level of theory using both LUNO (lowest unoccupied natural orbital) occupation number (POP = NO) and Yamaguchi's formula (table S2) (*45*). The spin locations were predicted from natural spin densities of Kohn-Sham MOs with the NBO6 program package.

SUPPLEMENTARY MATERIALS

Supplementary material for this article is available at http://advances.sciencemag.org/cgi/content/full/5/5/eaav2336/DC1

Fig. S1. Modified multigram synthesis of **M1**.
Fig. S2. ^{1}H and ^{13}C NMR of (**1**).
Fig. S3. ^{1}H and ^{13}C NMR of (**2**).
Fig. S4. ^{1}H NMR (600 MHz, $C_2D_2Cl_4$, 398 K) of the polymer.
Fig. S5. Solution and solid-state properties of the polymer.
Fig. S6. Stability studies of the polymer.
Fig. S7. Calculated data for the oligomers (n = 2 to 8) at the UB3LYP/6-31G** level of theory.
Fig. S8. Optimized ground-state geometric structures for the trimer (n = 3) and pictorial representations of the frontier MOs and spin density distribution.
Fig. S9. Optimized ground-state geometric structures for the tetramer (n = 4) and pictorial representations of the frontier MOs and spin density distribution.
Fig. S10. Optimized ground-state geometric structures for the hexamer (n = 6) and pictorial representations of the frontier MOs and spin density distribution.
Fig. S11. Bond length plots of the dimer (n = 2) singlet (orange) and triplet (blue) states.
Fig. S12. Bond length plots of the trimer (n = 3) singlet (orange) and triplet (blue) states.
Fig. S13. Bond length plots of the tetramer (n = 4) singlet (orange) and triplet (blue) states.
Fig. S14. Bond length plots of the hexamer (n = 6) singlet (orange) and triplet (blue) states.
Fig. S15. Bond length plots of the octamer (n = 8) singlet (orange) and triplet (blue) states.
Fig. S16. Chemical structures of polymers with various substitution patterns and calculated diradical character index (y) for the tetramers (n = 4).
Table S1. Inductively coupled plasma optical emission spectroscopy and x-ray photoelectron spectroscopy trace metal analysis.
Table S2. Selected electronic properties of oligomers as a function of the number of repeat units.
Table S3. Tabulated bond lengths for the octamer (n = 8).
Table S4. Tabulated bond lengths for the auxiliary rings of the octamer (n = 8).
Table S5. Tabulated NICS values of the dimer (n = 2).
Table S6. Tabulated NICS values of the trimer (n = 3).
Table S7. Tabulated NICS values of the tetramer (n = 4).
Table S8. Tabulated NICS values of the hexamer (n = 6).
Table S9. Tabulated NICS values of the octamer (n = 8).

REFERENCES AND NOTES

1. M. Abe, Diradicals. *Chem. Rev.* **113**, 7011–7088 (2013).
2. Y. Huang, E. Egap, Open-shell organic semiconductors: An emerging class of materials with novel properties. *Polym. J.* **50**, 603–614 (2018).
3. Z. Sun, Q. Ye, C. Chi, J. Wu, Low band gap polycyclic hydrocarbons: From closed-shell near infrared dyes and semiconductors to open-shell radicals. *Chem. Soc. Rev.* **41**, 7857–7889 (2012).
4. M. Nakano, Open-shell-character-based molecular design principles: Applications to nonlinear optics and singlet fission. *Chem. Rec.* **17**, 27–62 (2017).
5. Y. Morita, S. Nishida, T. Murata, M. Moriguchi, A. Ueda, M. Satoh, K. Arifuku, K. Sato, T. Takui, Organic tailored batteries materials using stable open-shell molecules with degenerate frontier orbitals. *Nat. Mater.* **10**, 947–951 (2011).

6. G. E. Rudebusch, J. L. Zafra, K. Jorner, K. Fukuda, J. L. Marshall, I. Arrechea-Marcos, G. L. Espejo, R. P. Ortiz, C. J. Gómez-García, L. N. Zakharov, M. Nakano, H. Ottosson, J. Casado, M. M. Haley, Diindeno-fusion of an anthracene as a design strategy for stable organic biradicals. *Nat. Chem.* **8**, 753–759 (2016).
7. S. J. Blundell, F. L. Pratt, Organic and molecular magnets. *J. Phys. Condens. Matter* **16**, R771–R828 (2004).
8. A. Rajca, Organic diradicals and polyradicals: From spin coupling to magnetism? *Chem. Rev.* **94**, 871–893 (1994).
9. S. Kumar, Y. Kumar, S. Keshri, P. Mukhopadhyay, Recent advances in organic radicals and their magnetism. *Magnetochemistry* **2**, 42 (2016).
10. N. M. Gallagher, J. J. Bauer, M. Pink, S. Rajca, A. Rajca, High-spin organic diradical with robust stability. *J. Am. Chem. Soc.* **138**, 9377–9380 (2016).
11. T. Y. Gopalakrishna, W. Zeng, X. Lu, J. Wu, From open-shell singlet diradicaloids to polyradicaloids. *Chem. Commun.* **54**, 2186–2199 (2018).
12. Y. Morita, S. Suzuki, K. Sato, T. Takui, Synthetic organic spin chemistry for structurally well-defined open-shell graphene fragments. *Nat. Chem.* **3**, 197–204 (2011).
13. G. Z. Magda, X. Jin, I. Hagymási, P. Vancsó, Z. Osváth, P. Nemes-Incze, C. Hwang, L. P. Biró, L. Tapasztó, Room-temperature magnetic order on zigzag edges of narrow graphene nanoribbons. *Nature* **514**, 608–611 (2014).
14. T. M. Swager, 50th anniversary perspective: Conducting/semiconducting conjugated polymers. A personal perspective on the past and the future. *Macromolecules* **50**, 4867–4886 (2017).
15. P. Ruffieux, S. Wang, B. Yang, C. Sánchez-Sánchez, J. Liu, T. Dienel, L. Talirz, P. Shinde, C. A. Pignedoli, D. Passerone, T. Dumslaff, X. Feng, K. Müllen, R. Fasel, On-surface synthesis of graphene nanoribbons with zigzag edge topology. *Nature* **531**, 489–492 (2016).
16. J. Casado, *Para*-quinodimethanes: A unified review of the quinoidal-versus-aromatic competition and its implications. *Top. Curr. Chem.* **375**, 73 (2017).
17. A. Narita, X.-Y. Wang, X. Feng, K. Müllen, New advances in nanographene chemistry. *Chem. Soc. Rev.* **44**, 6616–6643 (2015).
18. Y. Li, L. Li, Y. Wu, Y. Li, A review on the origin of synthetic metal radical: Singlet open-shell radical ground state? *J. Phys. Chem. C* **121**, 8579–8588 (2017).
19. P. Karafiloglou, The double (or dynamic) spin polarization in π diradicals. *J. Chem. Educ.* **66**, 816–818 (1989).
20. L. Salem, C. Rowland, The electronic properties of diradicals. *Angew. Chem.* **11**, 92–111 (1972).
21. A. Rajca, J. Wongsriratanakul, S. Rajca, Magnetic ordering in an organic polymer. *Science* **294**, 1503–1505 (2001).
22. P. M. Lahti, *Magnetic Properties of Organic Materials* (Taylor & Francis, 1999).
23. D. R. McMasters, J. Wirz, G. J. Snyder, 2,2-Dimethyl-2*H*-dibenzo[*cd,k*]fluoranthene, the first kekulé hydrocarbon with a triplet ground state. *J. Am. Chem. Soc.* **119**, 8568–8569 (1997).
24. W. Zeng, W. Zeng, H. Phan, T. S. Herng, T. Y. Gopalakrishna, N. Aratani, Z. Zeng, H. Yamada, J. Ding, J. Wu, Rylene ribbons with unusual diradical character. *Chem* **2**, 81–92 (2017).
25. G. Gryn'ova, M. L. Coote, C. Corminboeuf, Theory and practice of uncommon molecular electronic configurations. *Wiley Interdiscip. Rev. Comput. Mol. Sci.* **5**, 440–459 (2015).
26. J. D. Yuen, M. Wang, J. Fan, D. Sheberla, M. Kemei, N. Banerji, M. Scarongella, S. Valouch, T. Pho, R. Kumar, E. C. Chesnut, M. Bendikov, F. Wudl, Importance of unpaired electrons in organic electronics. *J. Polym. Sci. A* **53**, 287–293 (2015).
27. A. E. London, L. Huang, B. A. Zhang, M. B. Oviedo, J. Tropp, W. Yao, Z. Wu, B. M. Wong, T. N. Ng, J. D. Azoulay, Donor–acceptor polymers with tunable infrared photoresponse. *Polym. Chem.* **8**, 2922–2930 (2017).
28. M. E. Foster, B. A. Zhang, D. Murtagh, Y. Liu, M. Y. Sfeir, B. M. Wong, J. D. Azoulay, Solution-processable donor–acceptor polymers with modular electronic properties and very narrow bandgaps. *Macromol. Rapid Commun.* **35**, 1516–1521 (2014).
29. K. Susumu, T. V. Duncan, M. J. Therien, Potentiometric, electronic structural, and ground- and excited-state optical properties of conjugated bis[(porphinato)zinc(II)] compounds featuring proquinoidal spacer units. *J. Am. Chem. Soc.* **127**, 5186–5195 (2005).
30. Y. Joo, L. Huang, N. Eedugurala, A. E. London, A. Kumar, B. M. Wong, B. W. Boudouris, J. D. Azoulay, Thermoelectric performance of an open-shell donor–acceptor conjugated polymer doped with a radical-containing small molecule. *Macromolecules* **51**, 3886–3894 (2018).
31. A. Tsuda, A. Osuka, Fully conjugated porphyrin tapes with electronic absorption bands that reach into infrared. *Science* **293**, 79–82 (2001).
32. C.-K. Mai, R. A. Schlitz, G. M. Su, D. Spitzer, X. Wang, S. L. Fronk, D. G. Cahill, M. L. Chabinyc, G. C. Bazan, Side-chain effects on the conductivity, morphology, and thermoelectric properties of self-doped narrow-band-gap conjugated polyelectrolytes. *J. Am. Chem. Soc.* **136**, 13478–13481 (2014).
33. E. E. Havinga, W. ten Hoeve, H. Wynberg, Alternate donor-acceptor small-band-gap semiconducting polymers; Polysquaraines and polycroconaines. *Synth. Met.* **55**, 299–306 (1993).
34. B. Bleaney, K. D. Bowers, Anomalous paramagnetism of copper acetate. *Proc. R. Soc. Lond. A* **214**, 451–465 (1952).
35. A. Rajca, S. Utamapanya, D. J. Smithhisler, Near-degeneracy between the low- and high-spin states in an alternant hydrocarbon diradical: Topology and geometry. *J. Org. Chem.* **58**, 5650–5652 (1993).
36. K. J. Standley, *Electron Spin Relaxation Phenomena in Solids* (Springer, 2013).
37. H. Chen, A. G. Maryasov, O. Y. Rogozhnikova, D. V. Trukhin, V. M. Tormyshev, M. K. Bowman, Electron spin dynamics and spin-lattice relaxation of trityl radicals in frozen solutions. *Phys. Chem. Chem. Phys.* **18**, 24954–24965 (2016).
38. J. R. Klauder, P. W. Anderson, Spectral diffusion decay in spin resonance experiments. *Phys. Rev.* **125**, 912–932 (1962).
39. K. Kamada, K. Ohta, A. Shimizu, T. Kubo, R. Kishi, H. Takahashi, E. Botek, B. Champagne, M. Nakano, Singlet diradical character from experiment. *J. Phys. Chem. Lett.* **1**, 937–940 (2010).
40. Z. Zeng, M. Ishida, J. L. Zafra, X. Zhu, Y. M. Sung, N. Bao, R. D. Webster, B. S. Lee, R.-W. Li, W. Zeng, Y. Li, C. Chi, J. T. López Navarrete, J. Ding, J. Casado, D. Kim, J. Wu, Pushing extended p-quinodimethanes to the limit: Stable tetracyano-oligo(N-annulated perylene) quinodimethanes with tunable ground states. *J. Am. Chem. Soc.* **135**, 6363–6371 (2013).
41. R. Ponce Ortiz, J. Casado, V. Hernández, J. T. López Navarrete, P. M. Viruela, E. Ortí, K. Takimiya, T. Otsubo, On the biradicaloid nature of long quinoidal oligothiophenes: Experimental evidence guided by theoretical studies. *Angew. Chem. Int. Ed.* **46**, 9057–9061 (2007).
42. G. J. Snyder, Rational design of high-spin biradicaloids in the isobenzofulvene and isobenzoheptafulvene series. *J. Phys. Chem. A* **116**, 5272–5291 (2012).
43. A. D. Becke, A new mixing of Hartree–Fock and local density-functional theories. *J. Chem. Phys.* **98**, 1372–1377 (1993).
44. Z. Chen, C. S. Wannere, C. Corminboeuf, R. Puchta, P. v. R. Schleyer, Nucleus-independent chemical shifts (NICS) as an aromaticity criterion. *Chem. Rev.* **105**, 3842–3888 (2005).
45. K. Yamaguchi, H. Fukui, T. Fueno, Molecular orbital (MO) theory for magnetically interacting organic compounds. Ab-initio MO calculations of the effective exchange integrals for cyclophane-type carbene dimers. *Chem. Lett.* **15**, 625–628 (1986).

Acknowledgments

Funding: The work performed at The University of Southern Mississippi was made possible through the Air Force Office of Scientific Research (AFOSR) under support provided by the Organic Materials Chemistry Program (grant FA9550-17-1-0261, program manager: K. Caster) and was supported by the National Science Foundation (OIA-1757220, OIA-1632825, DGE-144999, and DMR-1726901), and we thank the AFOSR and NSF for this support. The EPR measurements at the University of Alabama were supported by the National Science Foundation (CHE-1416238). X.G. acknowledges financial support from the U.S. Department of Energy (DE-SC0019361) for the scattering aspect of the manuscript. N.R. and M.A.S. acknowledge financial support from the National Science Foundation (OIA-1430364 and OIA-1757220) for the computational aspects of the manuscript. DFT calculations were performed at The High Performance Computing Collaboratory at Mississippi State University. M.S. acknowledges financial support from the U.S. Department of Energy (DE-SC0002136). B.M.W. acknowledges financial support from the Office of Naval Research (grant N00014-18-1-2740) for computational aspects of the manuscript. Part of the materials synthesis was performed as a user project at the Molecular Foundry (Lawrence Berkeley National Laboratory) supported by the Office of Science and Office of Basic Energy Sciences of the U. S. Department of Energy under contract no. DE-AC02-05CH11231. Use of the SSRL (SLAC National Accelerator Laboratory) was supported by the U.S. Department of Energy (Office of Science and Office of Basic Energy Sciences) under contract no. DE-AC02-76SF00515. **Author contributions:** A.E.L. contributed to all the experimental work. H.C. and M.K.B. carried out the pulsed EPR experiments. B.A.Z., Y.L., J.T., and N.E. contributed to the synthesis. X.G. performed the x-ray measurement and data analysis. M.S. performed the SQUID measurements and data analysis. M.A.S., B.M.W., and N.R. performed the DFT simulations and analyzed the computational data. A.E.L., M.A.S., J.T., N.R., M.K.B., and J.D.A. wrote the manuscript. J.D.A. designed and directed the study. All authors commented on the paper. **Competing interests:** The authors declare that they have no competing interests. **Data and materials availability:** All data needed to evaluate the conclusions in the paper are present in the paper and/or the Supplementary Materials. Additional data related to this paper may be requested from the authors.

Submitted 27 August 2018
Accepted 15 April 2019
Published 24 May 2019
10.1126/sciadv.aav2336

Citation: A. E. London, H. Chen, M. A. Sabuj, J. Tropp, M. Saghayezhian, N. Eedugurala, B. A. Zhang, Y. Liu, X. Gu, B. M. Wong, N. Rai, M. K. Bowman, J. D. Azoulay, A high-spin ground-state donor-acceptor conjugated polymer. *Sci. Adv.* **5**, eaav2336 (2019).

Science Advances

A high-spin ground-state donor-acceptor conjugated polymer

A. E. London, H. Chen, M. A. Sabuj, J. Tropp, M. Saghayezhian, N. Eedugurala, B. A. Zhang, Y. Liu, X. Gu, B. M. Wong, N. Rai, M. K. Bowman and J. D. Azoulay

Sci Adv **5** (5), eaav2336.
DOI: 10.1126/sciadv.aav2336